Journal of Theoretical and Applied Information Technology
15th April 2022. Vol.100. No 7

ISSN: 1992-8645 www.jatit.org E-ISSN: 1817-3195

SPECTRAL UNMIXING WITH HYPERSPECTRAL IMAGES: A MULTI-OBJECTIVE LION OPTIMIZATION APPROACH

[1] RAJA NATARAJAN, [2] VADIVEL RAMASAMY
[1]Ph.D. Scholar, Department of Information Technology, Bharathiar University, Coimbatore, India
Assistant Professor (Computer Science), Tamil Nadu Agricultural University, Coimbatore, India
[2]Assistant Professor, Department of Information Technology, Bharathiar University, Coimbatore,
E-mail: [1]nraja@tnau.ac.in, [2]vlr_vadivel@yahoo.co.in

ABSTRACT

Spectral unmixing is an important phase in interpreting hyperspectral images to estimate the endmembers and their corresponding fractional abundances from the mixed pixels. Sparse unmixing approach is one among the promising spectral unmixing methods; however, noises impair hyperspectral images, indicating that the sparse unmixing model's performance getting degraded. This study uses a multi-objective lion optimization technique for spectral unmixing from hyperspectral satellite images to extract fractional abundances of valid endmembers from mixed pixels. To estimate the fractional abundances of each endmember, the proposed approach defines a multi-objective function which includes Euclidean and Frobenius norms and optimization variables that are associated with the abundance and mixing matrices. Based on the lion's social behaviors, the optimization function uses pride generation for finding solutions, mating for generating new solutions, territorial takeover and territorial defense to identify and remove worse solution by introducing a new optimum solution. The major objectives used in the objective functions are Spatial Neighbor, Sparsity, and Reconstruction Error. The proposed technique's performance is evaluated using Urban and Cuprite datasets with 06 and 12 endmembers respectively. In the investigations, the proposed methodology outperformed the Bilinear and Trilinear Multi-Objective Spectral Unmixing, Robust Collaborative Nonnegative Matrix Factorization, Pareto-Multi-Objective Spectral Unmixing, and Rider Optimization methods in estimating the enhanced endmembers and their corresponding fractional abundances with lower reconstruction error and root mean square error values of 119.11 and 0.0904, respectively.

Keywords: *Spectral Unmixing, Hyperspectral Images, Multi-Objective Optimization, Endmembers*

1. INTRODUCTION

Hyperspectral imaging [1] is a remote sensing technique that collects multi-dimensional data cubes made up of two-dimensional spatial images acquired in many contiguous spectral bands. Agricultural monitoring, terrain classification, military surveillance, and environmental monitoring are just a few of the applications for hyperspectral imaging. Imaging spectroscopy is another name for hyperspectral imaging. It generates images by combining numerous narrow-band spectral bands with a few nanometer resolution. The spectral band uses visible and near-infrared wavelengths up to 2.5 micro meters. Because hyperspectral sensors can distinguish visually similar surface resources, each substance has its own reflectance spectrum [2]. Hyperspectral imaging is a type of imaging that analyses and collects data from the electromagnetic spectrum. Hyperspectral photos contain high-resolution spectral information for earth observation and geoinformation science. Furthermore, mixed pixels arise in hyperspectral data due to lower spatial resolution, microscopic particles, and different scattering [3]. Because the sensor utilised has a lower spatial resolution, each pixel of the recorded spectra contains more than one spectral signature when the hyperspectral picture lies over solid surfaces [4]. Spectral Unmixing (SU) have received a lot of attention in the signal processing and imaging literature during the last few decades [5]. The technique of Spectral Unmixing (SU) is used to solve common hyperspectral imaging problems. Among the challenges are material quantification, sub-pixel detection, and pixel categorization. SU entails dissecting a pixel spectrum into material spectra, known as endmembers, and determining the abundances or fractions of the endmembers [6]. SU comprises macroscopic materials in a picture, which are quantified in image pixels. The sum of component spectra is used by the majority of SU approaches to calculate pixel reflectance [7,8]. In SU, the pixel spectrum is blended with pure component spectra, and a percentage is utilised to represent the proportion of each endmember in a pixel. Depending on the hyperspectral image, the spectral unmixing picture is related to a nonlinear or linear mixture model [9]. In spectral unmixing research, the Linear Mixture Model (LMM) has been widely used [10,11]. Many typical algorithms for finding endmember signatures for spectral unmixing purposes have been created using this concept, including the N-finder algorithm [11,12], iterative error analysis, Vertex Component Analysis (VCA) [11,13], and pixel purity index [11,14]. Canonical Correlation Analysis is used in [15,16] to emphasise the multiple-change information utilising an unsupervised Multivariate Alteration Detection (MAD) approach (CCA).

The major goal of this study is to design and build a method for using hyperspectral satellite images in the SU. To determine fractional abundance of each endmember, LA is used in conjunction with a linear sparse unmixing model. To maximise the reconstruction term in the objective function, LA uses numerous objectives, including the sparsity term and the total variation regularisation term. The paper's main contribution is the use of LA for optimal end-member estimation. The fractional abundance of the endmember is optimally determined using the LA to increase global convergence and ensure local optimal avoidance, consequently improving the multi-objective functions of the proposed technique, such as SNI, SPA, and RE. This research paper is organised as follows: Section 1 contains an overview of the paper. The literature study is presented in part 2, and the approach for spectral unmixing utilising the LA is presented in section 3. The proposed method's findings and comments are depicted in Section 4, and the conclusion is presented in Section 5.

2. REVIEW OF LITERATURE

For handling sparse unmixing challenges, Xia Xu and Zhenwei Shi [17] created the Multi-objective Optimization based Sparse Unmixing (MOSU) algorithm. Sparse unmixing is transformed into a bi-objective issue via MOSU. The endmember sparsity and reconstruction error are the goals. Sparse unmixing is handled straight here, with no relaxing. For resolving subset selection difficulties, the devised unmixing strategy is aided by Pareto optimization (POSS). Then, in order to improve computing efficiency, POSS is extended to a population-based technique. More strategies for solving the sparse unmixing problem were not included in the method. For nonlinear spectral unmixing, Wenfei Luo et al. [11] devised bilinear spectral unmixing based on Particle Swarm Optimization (PSO) of hyperspectral pictures. For resolving challenges in the minimization technique for SU, a multi-objective optimization approach is presented; hence, constraints owing to penalty factors are eliminated. A number of complicated non-linear models and estimating parameters were required for the procedure. For the limiting complexity of linear SU approaches, Simon Henrot et al. [18] devised LMM using multi-temporal hyperspectral pictures. An efficient SU technique for reconstructing abundance maps and source spectra is devised using this model. On genuine multi-temporal hyperspectral images, the approach's performance is proved. The Multitemporal Spectral Unmixing (MSU) technique was presented by Sicong Liu et al. [16] to evaluate various change detection concerns in bit temporal HS pictures. The Change Detection (CD) problem is investigated in the multi temporal domain, using a bit temporal model to assess the spectral composition of a pixel. The automatic and unsupervised approach is used to extract Multi-temporal Endmembers (MT-EMs). The change analysis technique is then modelled in order to distinguish between change and no-change MT-EMs. Finally, the change detection problem is answered by looking at the different classes and how they contribute to each pixel. The major challenges are emphasized and listed below.

2.1 Challenges

Biswarm Particle Swarm Optimization (BiPSO) [11] is a technique for reducing the number of particles in a swarm. For nonlinear

ISSN: 1992-8645 www.jatit.org E-ISSN: 1817-3195

spectral unmixing, bilinear unmixing is used. This method can simply be transformed into a global search algorithm using Multistart and Random PSO. In actual applications, however, the process of converting to a global optimization technique is time-consuming. There's also a need to think about global search strategies and mathematical verification. Because of the poor spatial resolution of the mixes and sensors obtained at different scales, the multi-objective cooperative convolutionary approach [19] confronts a substantial issue in recognising the endmember signatures. The present sparse unmixing has the disadvantage that the current spectral signature in the scene must be the same as its corresponding sample in the spectral library, which is an unrealistic assumption in the real world, resulting in detrimental effects [6]. Iterative Reweighted Multivariate Alteration Detection (IR-MAD) was introduced in [20], and it necessitates a strong involvement with the end users to pick the most informative components that represent the precise alterations of interest, which is always time demanding. As a result, using it to detect all possible change classes is difficult, especially when the overall number of changes is large. To handle sparse unmixing problems, the Multi-objective Optimization based Sparse Unmixing method (MOSU) was introduced in [17]. The sparse unmixing task is difficult because it is transformed into an NP-hard norm based on an optimization problem. To identify the original norm, the method commonly employs a relaxation. As a result, more computation error and sensitive weighted parameters may result from the relaxation.

The multi-fidelity evolutionary multitasking optimization (MFEMO) framework is proposed to resolve the challenges in endmember extraction from the influence of outliers and expensive computation respectively. However, MFEMO includes inevitable negative transfer between tasks during endmember extraction which deteriorate the accuracy of endmember estimation [26]. To solve large-scale sparse unmixing challenges, an evolutionary multi-objective hyperspectral sparse unmixing algorithm with endmember priori method (EMSU-EP) is deviced. However this method has challenges in controlling the noise in the large scale sparse unmixing problems [27]. A multiobjective-based simultaneous sparse unmixing framework (PMoSU) where reconstruction error, sparsity error, and the pruning projection function are considered as three parallel objectives for spectral unmixing, which works under high-noise conditions. In the context of discrete range of sparse unmixing may lead to weakly Pareto optimal solutions [28].

3. PROPOSED METHODOLOGY

The spectra of a mixed pixel is measured using SU, which is divided into several constituent spectra and a set of corresponding abundances or fractions to show the proportion of each endmember in the pixel. In spectral unmixing, there are three major steps. The endmembers are initially computed from a image. Following that, the spectral signatures are recognised, and the fractional abundance of each endmember connected to a single pixel is computed. Although all prior works followed these processes, there are inaccuracies and propagation problems in the current works when computing the endmember. The endmember and the fraction of the signature are initially approximated using LA [21]. The computation of fractional abundance is constrained using a multi-objective function based on RSE, SPA, and SNI to increase estimation accuracy. Figure 1 shows a schematic illustration of the suggested spectral unmixing model.

In matrix form, the hyperspectral image is represented as,

$$M = \{m1,\dots,mj\} \in Q^{v\times j} \mathrm{M} = \{\mathrm{m}_1,\dots,\mathrm{m}_j\} \in \mathrm{Q}^{v\times j} \quad (1)$$

where$j$denotes the total spectra vectors, and v denotes the spectral bands in the hyperspectral image. The input image is expressed using the Linear Mixture Model (LMM) as,

$$M = \mathrm{Y}k + J \text{such that} k \geq 0 1_r^s k = 1_j^s \quad (2)$$

where, the mixing matrix is denoted as, $Y = [y_1,\dots,y_l,\dots,y_r] \in Q^{v\times r}$with rr endmembers, $y_l$indicates the l^{th}l$^{\mathrm{th}}$signature of the endmember and the noise that affects the measuring process is JJ. The abundance matrix is represented as$k$k, which in matrix form is expressed as,

$$k = [x_1,\dots,x_l,\dots,x_j] \in Q^{r\times j} \quad (3)$$

The abundance matrix contains fractions of the endmembers and $\mathrm{x_l x_l}$ be the $\mathrm{l^{th} l^{th}}$fraction of endmember in such a way that the pixel ll varies between 1 and jj. The endmembers component-wise enables the best understanding of the abundance non-negativity constraint, which is represented as $\mathrm{k} \geq 0\mathrm{k} \geq 0$. On the other hand, $1_r^S\mathrm{k} = 1_j^S 1_r^s\mathrm{k} = 1_j^s$ implies the sum-to-one constraint of the abundance vector for physical interpretation, and $1_r = 1_\mathrm{r} =$

$[1,1,\ldots,1]^S$specifies column vector of dimension rr. The transpose of the vector elements is denoted as $[\quad]^T$. Assume that out of the rr endmembers, ss endmembers are calculated using total endmembers and estimated endmembers. When rr and s are similar, ideal situation arise, while $s < rs < r$ shows the underestimated state of the endmembers. The second condition identifies more number of endmembers. The computation of rr, YY, and kk is performed using optimization algorithm based on multi-objective function.

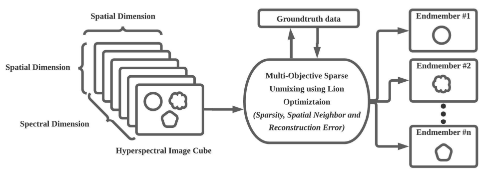

Figure 1. Conceptual flow diagram of Multi-Objective Sparse Unmixing using Lion Optimization

3.1 Generation of Multi-Objective Function

The objective function estimates the endmembers and their abundance factor using SNI, SPA and RSE respectively. The following formula is used to model the objective function,

$$\min_{U,V}\left\{\frac{1}{2}\|M-\mathrm{UV}\|_G^d + \in \|V\|_{2,1} + \frac{\eta}{2}\|U - K\|_G^d\right\} \min_{\mathrm{U,V}}\left\{\frac{1}{2}\|\mathrm{M\text{-}UV}\|_{\mathrm{G}}^{\mathrm{d}} + \varepsilon\|\mathrm{V}\|_{2,1} + \frac{\eta}{2}\|\mathrm{U\text{-}K}\|_{\mathrm{G}}^{\mathrm{d}}\right\} \quad (4)$$

$$\text{such that } \mathrm{V} \in \Omega_{\mathrm{s\text{-}1}}\mathrm{U} \in \mathrm{F}_{\mathrm{s\text{-}1}} V \in \Omega_{s-1} U \in F_{s-1}$$

where, $\|\ \|_2\|\ \|_2$and $\|\ \|_G\|\ \|_G$signifies the Euclidean and Frobenius norms, respectively. $\mathrm{U} \equiv [h_1,\ldots,h_s] \in Q^{v\times s}\mathrm{U} \equiv [h_1,\ldots,h_s] \in Q^{v\times s}$ and $V \in Q^{s\times j}\mathrm{V} \in Q^{s\times j}$indicates the optimization variables that are connected with the abundance matrix and mixing matrix. Data fidelity $\|\mathrm{M\text{-}UV}\|_G^d\|\mathrm{M\text{-}UV}\|_G^d$that promote solution with low reconstruction errors and $\frac{\eta}{2}\|U - K\|_G^d \frac{\eta}{2}\|\mathrm{U\text{-}K}\|_G^d$drags the column in Utowards the solutionKK, that along with the matrix VVpulls the endmembers to the extreme that, is described by dataMM.$\|\mathrm{V}\|_{2,1}\|\mathrm{V}\|_{2,1}$ enables the row sparsity for the matrix VV through setting the complex rows at zero. The SPA is given as,

$$\|\mathrm{V}\|_{2,1} = \textstyle\sum_{i=1}^{s}\|a\|_2\ \|\mathrm{V}\|_{2,1} = \sum_{i=1}^{s}\|\alpha\|_2 \quad (5)$$

Equation (5) specifies the mixed norm belongs to matrix VV. The SNI is formulated as

$$\mathrm{SNI} = \frac{\eta}{2}\|U - k\|_G^d \mathrm{SNI} = \frac{\eta}{2}\|\mathrm{U\text{-}K}\|_{\mathrm{G}}^{\mathrm{d}} \quad (6)$$

where, $\mathrm{K} = [m_{i_1},\ldots,m_{i_s}]\mathrm{K} = [m_{i_1},\ldots,m_{i_s}]$ indicates the set of ssspectral vectors. The constants, ηη and εεare the regularization parameters. $\Omega_{s\text{-}1}\Omega_{s\text{-}1}$ be the total dimension matrix of $(s\times j)(s\times j)$, and the columns are of size $(s\text{-}1)(s\text{-}1)$. Similarly, $F_{s\text{-}1}F_{(s\text{-}1)}$are the matrix collections with size $(u\times s)(u\times s)$. The objective function solves the issues associated with the violation of the sum-to-one constraints that is generally available in real data.

3.2 Estimation of Fractional Abundances for Each Endmember

The Lion Optimization Algorithm [21] is discussed in this section for calculating the fractional abundance of the endmember. The LA looks for the best solution based on lion behaviour like territorial takeover and territorial defence. The territorial defence is carried out by nomadic and resident males, whereas the territorial conquest is carried out by new and old territorial males. Pride formation, mating, territorial defence, and territorial takeover are all processes in the Lion Optimization Algorithm. Pride generation is used to find solutions, while mating is used to find new ones, and territorial takeover is used to find and replace the worst solution with a better one. The phases of the Lion Optimization Algorithm are depicted in the diagram below.

3.2.1 Pride generation

First, Pride generation is defined as $Y^{male}Y^{male}$, $Y^{female}Y^{female}$, $Y^{nomad}Y^{nomad}$ of which, $Y^{male}Y^{male}$and$Y^{female}Y^{female}$create pride. The vector elements of $Y^{male}Y^{male}$, $Y^{female}Y^{female}$ and $Y^{nomad}Y^{nomad}$ i.e, $Y^{male}y^{male}(t)$, $Y^{female}y^{female}(t)$, and $Y^{nomad}y^{nomad}$ are arbitrary integers in the maximum and minimum limits, where $t = 1,2,\ldots,Tt = 1,2,\ldots,T$. Here, Tindicates the total number of fractional abundance of endmembers to be optimized.

3.2.2 Evaluation of objective function

Male, female, and nomad lions' fitness is determined using equation (4) and they are represented as $F(Y^{male})F(Y^{male})$, $F(Y^{female})F(Y^{femele})$, and $F(Y^{nomad})F(Y^{nomad})$. For the following steps, consider $F^{ref} = F(Y^{male})F^{ref} = F(Y^{male})$and $R_f = 0$, where

ISSN: 1992-8645 www.jatit.org E-ISSN: 1817-3195

$\mathrm{R_f R_j}$indicates the generation counter that is utilized for testing the termination condition.

3.2.3 Evaluation of fertility

The productiveness of the territorial lioness and lion is determined by this mechanism. In addition, the fertility evaluation method is used to create an updated female lion, termed as $Y^{\text{female}+}\mathrm{Y^{female+}}$.

$$Y^{\text{female}+}=\{Y_p^{\text{female}+;\text{if}p=q}\ \mathrm{Y^{female+}}=\{\mathrm{y_p^{female+;ifp=q}} \quad (7)$$

where, $q$denotes the random integer. $Y_q^{\text{female}+}\mathrm{y_q^{female+}}$and $Y_p^{\text{female}+}\mathrm{y_p^{female+}}$ are the $\mathrm{q^{th}}q^{\text{th}}$, and p^{th}elements of$\mathrm{Y^{female+}Y^{female+}}$.

$$Y_p^{\text{female}+}=\min\left[y_p^{\max},\max\left(y_p^{\min},\nabla_p\right)\right]$$
$$\mathrm{y_p^{female+min\lfloor y_p^{max},max(y_p^{min},\nabla_p)\rfloor}} \quad (8)$$

$$\nabla p=\left|\begin{matrix} Y_p^{\text{female}}+(0.1r_2-o.o5) \\ \left(Y_p^{\text{male}}-r1y_p^{\text{female}}\right)\end{matrix}\right|$$
$$\nabla_{\mathrm{p}}=\lfloor \mathrm{y_p^{female}}+ \quad (9)$$
$$(0.1\mathrm{r_2}\text{-}0.05)\left(\mathrm{y_p^{male}}\text{-}\mathrm{r_1 y_p^{female}}\right)$$

where, the female update is represented as$\nabla\nabla$, and the random integers are denoted as $\mathrm{r_1}r_1\mathrm{r_2}$and r_2.

3.2.4 Mating

In this procedure, the new best solution is derived from the old solutions. There are two main steps in this phase: mutation and crossover. Four cubs, $Y^{\text{cubs}}$are produced from the crossover phase, and each cub is generated using a uniformly distributed random crossover probability P_r.

$$Y^{\text{cubs}}(p)=D_p^{\circ}Y^{\text{male}}+\overline{D_p^{\circ}}Y^{\text{female}}$$
$$\mathrm{Y^{cubs}(p)=D_p{\circ}Y^{male}+\overline{D_p}{\circ}Y^{female}} \quad (10)$$

where, DDdenotes the crossover mask, and $\overline{\mathrm{DD}}$be the one's complement of$D$. $\mathrm{Y^{cubs}Y^{cubs}}$are given to the mutation in an uniform manner with the probability rate N_r. From the mutation phase, new cubs are generated. The next step is gender clustering, where the male cub $Y^{\text{mcub}}\mathrm{Y^{mcub}}$ and female cub $Y^{\text{fcub}}\mathrm{Y^{fcub}}$ are extracted from the cub pool using primary and secondary best fitness. Once the male cub and female cub are chosen, their ages, denoted as$B_{\text{cub}},\mathrm{B_{cub}}$ are fixed to zero.

3.2.5 Cub growth function

In Cub Growth phase, $Y^{\text{mcub}}\mathrm{Y^{mcub}}$and $Y^{\text{fcub}}\mathrm{Y^{fcub}}$are fed to uniform mutation with the rate of$\mathrm{U_r U_r}$. At every update, if the mutated cub is better than the old cub, and the ages of $B_{\text{cub}}\mathrm{B_{cub}}$ of new cubs are increased by one, when the mutated cub replaces the old cub.

3.2.6 Territorial defense

One of the first lion operators is territorial defence, which is used to analyse the search space in a broader sense. The territorial defence is divided into three sections: pride, survival, and Nomad coalition updates. It is performed using subsequent Y^{nomad}. The winning nomad is selected based on the below equation,

$$F\left(Y^{e_{\text{nomad}}}\right)<F\left(Y^{\text{male}}\right) \quad (11)$$
$$F\left(Y^{e_{\text{nomad}}}\right)<F\left(Y^{m_{\text{cub}}}\right) \quad (12)$$
$$F\left(Y^{e_{\text{nomad}}}\right)<F\left(Y^{f_{\text{cub}}}\right) \quad (13)$$

When Y^{male} is defeated in the territorial defense, pride is updated by replacing $Y^{\text{male}}\mathrm{Y^{male}}$ by $Y^{e_{\text{nomad}}}$ conquer the nomad coalition, it is updated by selecting only one $Y^{\text{nomad}}\mathrm{Y^{nomad}}$. This procedure selects $Y_1^{\text{nomad}}\mathrm{Y_1^{nomad}}$, if $E_1^{\text{nomad}}\geq e\mathrm{E_1^{nomad}}\geq \mathrm{e}$ is fulfilled, or else select $Y_2^{\text{nomad}}\mathrm{Y_2^{nomad}}$and $e$represents the exponential of unity. $E_1^{\text{nomad}}\mathrm{E_1^{nomad}}$is computed using the below equation,

$$E_1^{\text{nomad}}=\exp\left(\frac{b1}{\max(b1,b2)}\right)\max\frac{\left(F\left(Y_1^{\text{nomad}}\right),F\left(Y_2^{\text{nomad}}\right)\right)}{F\left(Y_1^{\text{nomad}}\right)} \quad (14)$$

where, the Euclidean distance is represented as $b_1\mathrm{b_1}$ between the pair $\left(Y_1^{\text{nomad}},Y^{\text{male}}\right)\left(\mathrm{Y_1^{nomad}},\mathrm{Y^{male}}\right)$ and $\mathrm{b_2 b_1}$signifies the Euclidean distance between the pair $\left(Y_2^{\text{nomad}},Y^{\text{male}}\right)\left(\mathrm{Y_2^{nomad}},\mathrm{Y^{male}}\right)$, respectively. If the defense output is zero, $Y^{\text{male}}\mathrm{Y^{male}}$, and $F\left(Y^{\text{male}}\right)\mathrm{F}\left(\mathrm{Y^{male}}\right)$are saved, and from fertility evaluation, the process is repeated.

3.2.7 Territorial takeover

It takes place while the circumstance $B_{\text{cub}}\geq B_{\max}\mathrm{B_{cub}}\geq\mathrm{B_{max}}$is satisfied or else it will repeat the process from cub growth function. This process gives territory to $Y^{\text{mcub}}$and $Y^{\text{fcub}}\mathrm{Y^{fcub}}$once they grown and develops into stronger than $Y^{\text{male}}\mathrm{Y^{male}}$, and $Y^{\text{female}}\mathrm{Y^{female}}$.

3.2.8 Termination criteria

The above steps are repeated until it fulfills $\boldsymbol{N_f}>\boldsymbol{N_f^{\max}}\mathrm{N_f}>\mathrm{N_f^{\mathbf{max}}}$ where, the total number of function evaluations is denoted as $\boldsymbol{N_f}\mathrm{N_f}$, and $\boldsymbol{N_f^{\max}}\mathrm{N_f^{\mathbf{max}}}$denotes the maximum number of function evaluations.

Journal of Theoretical and Applied Information Technology
15th April 2022. Vol.100. No 7

ISSN: 1992-8645 www.jatit.org E-ISSN: 1817-3195

4. RESULTS AND DISCUSSION

This section dealt with the results and explanation of the suggested spectral unmixing method for computing the fractional abundance of endmembers. The proposed method's performance is compared to that of earlier efforts using metrics.

4.1. Experimental Arrangement

The proposed technique is implemented in MATLAB and runs on a computer with 4GB of RAM, Windows OS, and an Intel Core i3 processor.

4.2. Dataset Description

Urban and Cuprite data from [22] were used for the spectral unmixing. The urban data consists of approximately 307 x 307 pixels in a [2x2] metre square area, with 210 wavelengths ranging from 2500 nm to 400 nm with a spectral resolution of 10 nm. There are about three variants of ground truth for this urban data, 4, 5, and 6 endmembers, which are introduced in the ground truth. The ground truth of Urban dataset is opted with a six-end-members version. The six endmembers are Asphalt, Metal, Roof, Grass, Dirt, and Tree. Cuprite data is divided into 224 channels with wavelengths ranging from 370 to 2480 nm. The region under consideration is 250 × 190 pixels and contains 14 mineral types. There are small differences between the variants of similar minerals, and hence, there are 12 endmembers, such as Alunite, Buddingtonite, Andradite, Kaolinite1, Sphene, Dumortierite, Muscovite, Nontronite, Kaolinite2, Montmorillonite, Pyrope, and Chalcedony are the identified ground truth data of Cuprite dataset.

4.3. Experimental Setup

The results of the experiment are shown in this part, which includes the original Urban and Cuprite images, as well as their original endmembers and predicted endmembers based on LA-based spectral unmixing. Figure 2 displays the Urban and Cuprite Hyspectral Image Cubes.

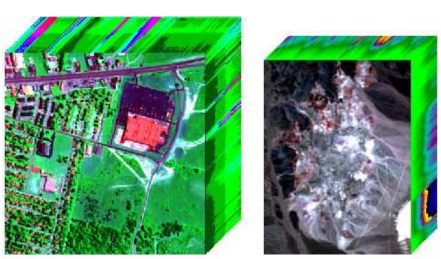

Figure 3 depicts the original endmembers that match to Urban hyperspectral image, and there are six endmembers version is used from (22). Figure 3a, Figure 3b, Figure 3c, Figure 3d, Figure 3e, and Figure 3f show the six original endmembers of Urban Image.The six estimated endmembers of the Urban are depicted in Figure 4. Figure 4a, figure 4b, Figure 4c, Figure 4d, Figure 4e, and Figure 4f.

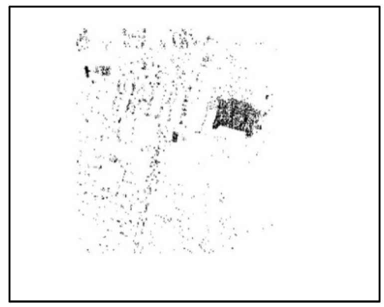

3a. Asphalt

3b. Grass

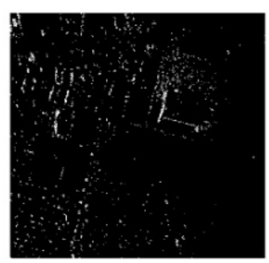

3c. Tree

3d. Roof

ISSN: 1992-8645 www.jatit.org E-ISSN: 1817-3195

3e. Metal

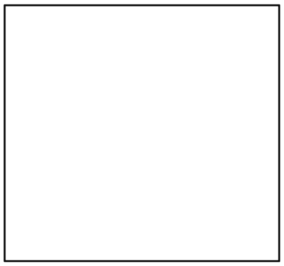

3f. Dirt

Figure 3. Original endmembers corresponding to Urban Hyperspectral Image,
3a. Asphalt, 3b. Metal 3c. Roof 3d. Grass 3e. Dirt 3f. Tree

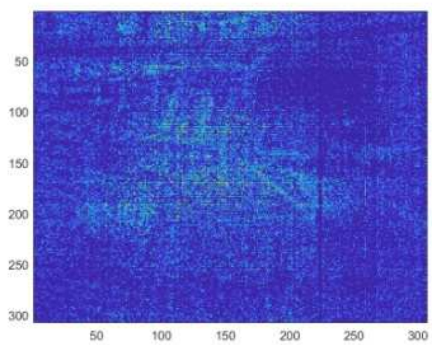

4a. Asphalt

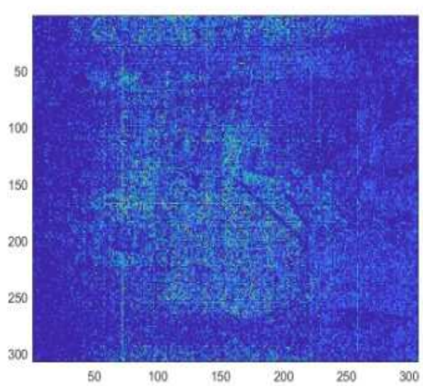

4b. Metal

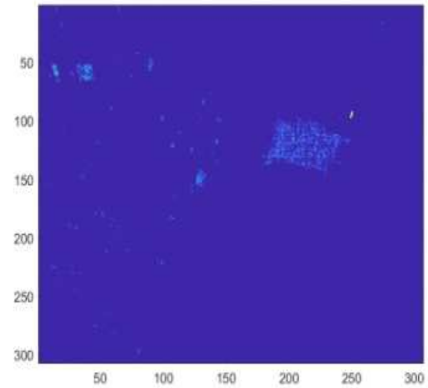

4c. Roof

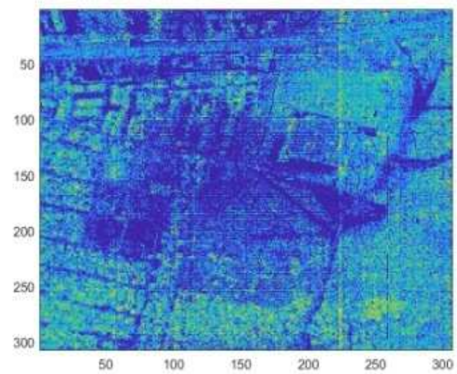

4d. Grass

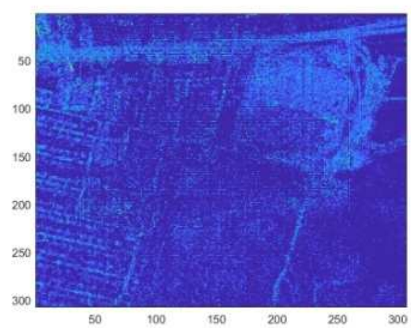

4e. Dirt

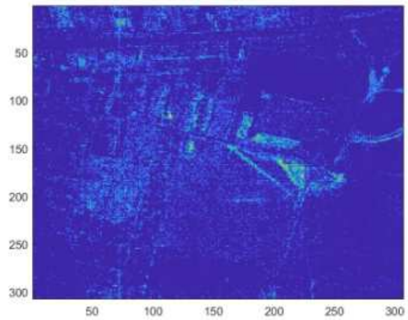

4f. Tree

Figure 4 Estimated endmembers corresponding to Urban Hyperspectral Image, 4a. Asphalt, 4b. Metal 4c. Roof 4d. Grass 4e. Dirt 4f. Tree

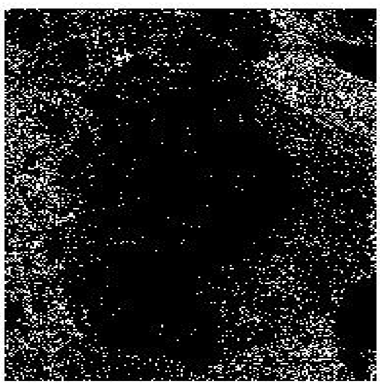

5a. Alunite

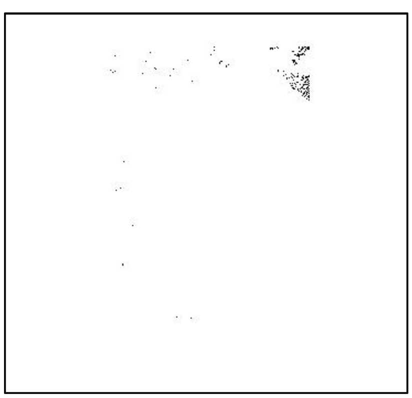

5b. Andradite

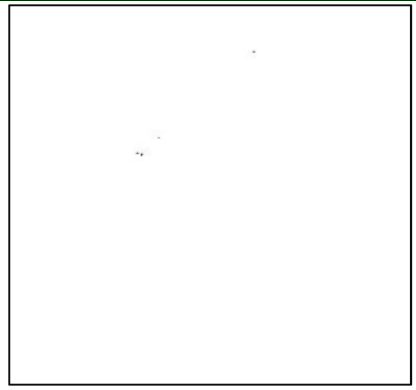

5c. Buddingtonite

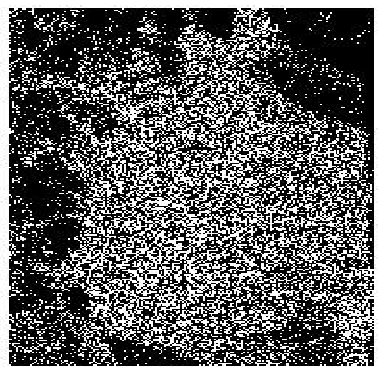

5d. Dumortierite.

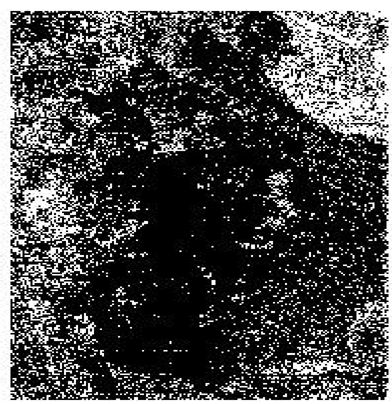

5e. Kaolinite1

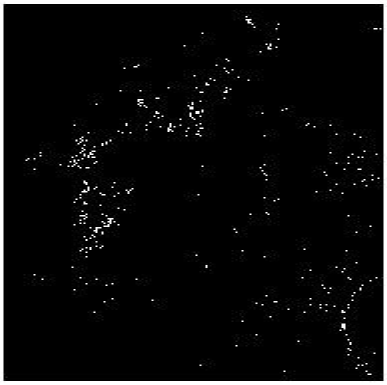

5f. Kaolinite2

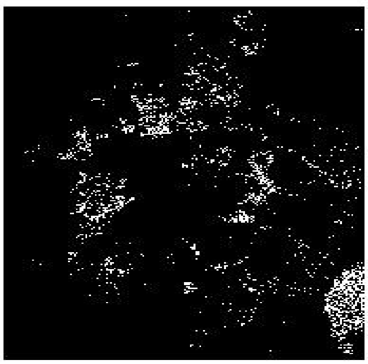

5g. Muscovite.

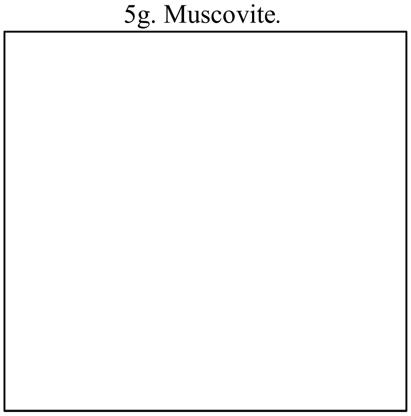

5h. Montmorillonite

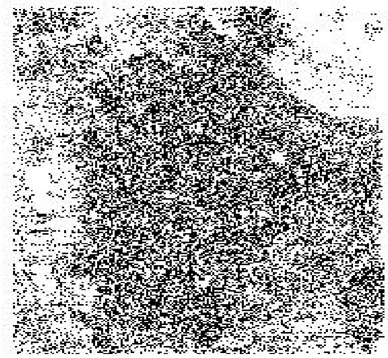

5i. Nontronite

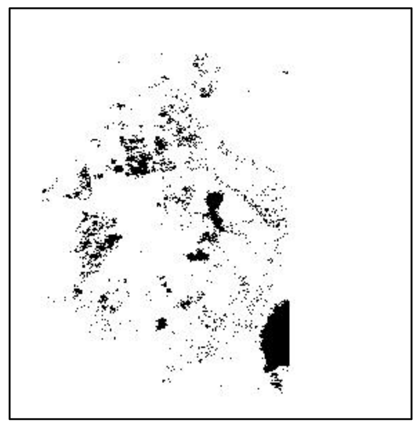

5j. Pyrope

15th April 2022. Vol.100. No 7

ISSN: 1992-8645 www.jatit.org E-ISSN: 1817-3195

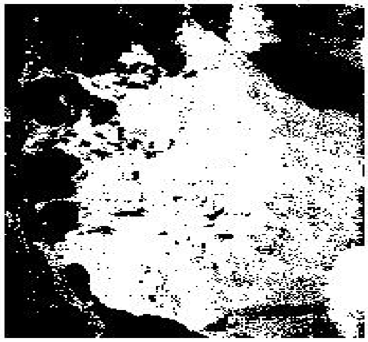

5k. Sphene

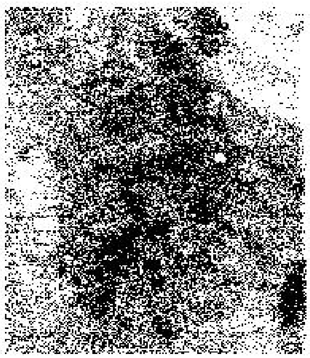

5l. Chalcedony

Figure 5. Original endmembers corresponding to Cuprite Hyperspectral Image, 5a. Alunite, 5b.Andradite, 5c.Buddingtonite, 5d. Dumortierite, 5e.Kaolinite1, 5f. Kaolinite2, 5g. Muscovite, 5h.Montmorillonite, 5i.Nontronite, 5j.Pyrope, 5k.Sphene, 5l.Chalcedony

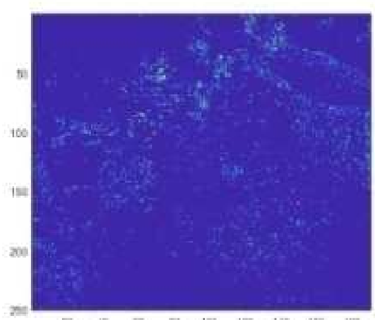

6a. Alunite

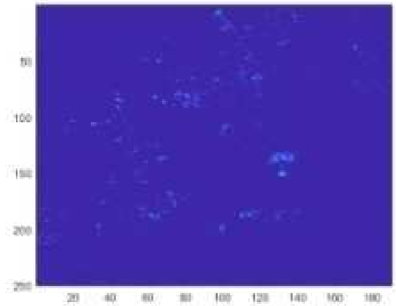

6b. Andradite

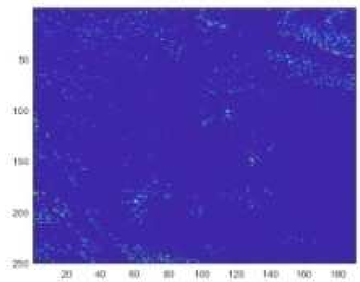

6c. Buddingtonite

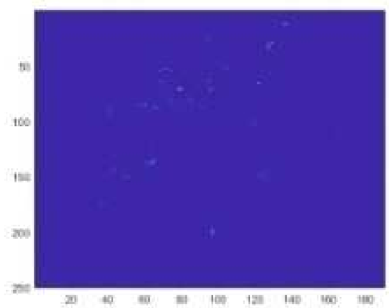

6d. Dumortierite

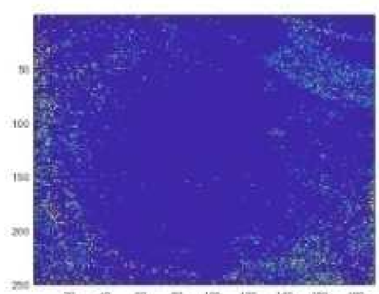

6e. Kaolinite1

ISSN: 1992-8645 www.jatit.org E-ISSN: 1817-3195

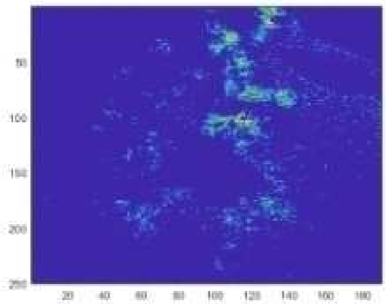

6f. Kaolinite2

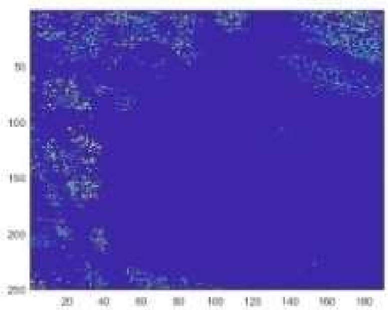

6g. Muscovite

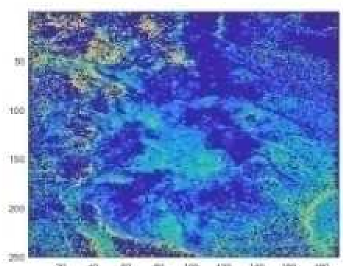

6h. Montmorillonite

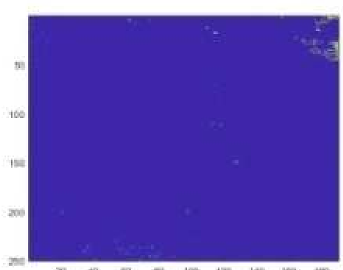

6i. Nontronite

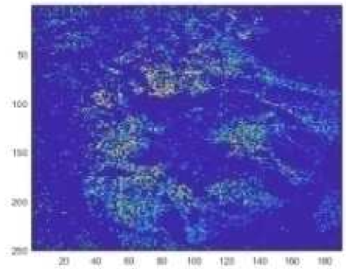

6j. Pyrope

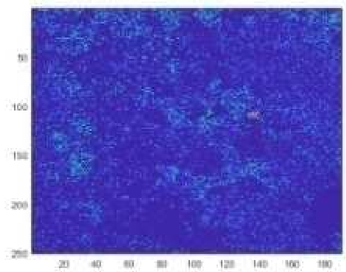

6k. Sphene

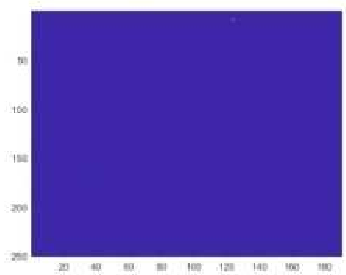

6l. Chalcedony

Figure 6Estimated endmembers corresponding to Cuprite Hyperspectral, 6b.Andradite, 6c.Buddingtonite, 6d. Dumortierite, 6e.Kaolinite1, 6f. Kaolinite2, 6g. Muscovite, 6h.Montmorillonite, 6i.Nontronite, 6j.Pyrope, 6k.Sphene, 6l.Chalcedony

4.4. Evaluation Metrics

The recommended technique's performance is measured using two metrics: RMSE and RE. The RMSE of the methods is calculated as follows,

$$\mathrm{RMSE}_j = \sqrt{\frac{1}{v}\sum} \qquad (15)$$

where, v refers to the total pixel, $y_{ij}y_{ij}y_{ij}$signifies the real abundance fraction for i^{th}endmember in $j^{th}j^{th}$pixel, and $\hat{y}_{ij}$refers to the corresponding estimated value. Thus,

$$\mathrm{RMSE} = \sqrt{} \qquad (16)$$

where, qq symbolizes the extracted endmembers and $\mathrm{RMSE}_j\mathrm{RMSE}_j\mathrm{RMSE}_j$corresponds to the RMSE of the individual pixels. The reconstruction error is computed as,

$$\mathrm{RE} = \|Z - \hat{Z}\|^2 \qquad (17)$$

where, Zrefers to the true abundance matrix and $\hat{Z}$ indicates the estimated abundance matrix.

The following table explains the performance analysis of the proposed algorithm to calculate the fractional abundances using the endmembers with respect to the bands selected. Table 1 shows that the percentage of the original fractional abundances (in y axis) of endmembers (in x axis) #1 through #6 (of Asphalt, Metal, Roof, Grass, Dirt and Tree) of Urban image for the varying population size 5 to 25 in spectral band 50.

Table 1. Performance analysis of LOA in calculating the original fractional abundances using Urban Image at band size 50

Endmember	LOA Population 5	LOA Population 10	LOA Population 15	LOA Population 20	LOA Population 25
#1	0.0045	-0.0606	0.0359	-0.0001	0
#2	0.0102	-0.0002	0.0052	0.0008	0.0004
#3	0.0174	0.0063	0.0019	0.0002	0.0281
#4	-0.0008	0.0067	0.0253	0	0.0134
#5	0.0033	-0.0087	-0.0085	-0.0004	0.0039
#6	0.0049	-0.0019	0.0415	0.0149	0.0377

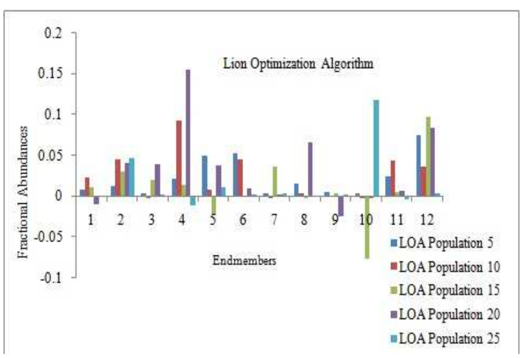

Figure 7 Performance analysis offractional abundances of endmembers (#1 Asphalt, #2 Metal, #3 Roof, #4 Grass, #5 Dirt and #6 Tree) corresponding to Urban Image

Table 2 shows that the performance analysis of endmembers #1 through #12 (of Alunite, Andradite, Buddingtonite, Dumortierite, Kaolinite1, Kaolinite2, Muscovite, Montmorillonite, Nontronite, Pyrope, Sphene and Chalcedony) of Cuprite image for the varying population size 5 to 25 in spectral band 50.

Table 2. Performance analysis of LOA in calculating the original fractional abundances using Cuprite Image at band size 50

Endmember	LOA Population 5	LOA Population 10	LOA Population 15	LOA Population 20	LOA Population 25
#1	0.0089	0.0237	0.0118	-0.0087	0.0004
#2	0.0134	0.0453	0.0303	0.0406	0.0465
#3	0.0045	-0.0004	0.0209	0.0398	0.0027
#4	0.022	0.0929	0.0137	0.1552	-0.012
#5	0.05	0.008	-0.0228	0.0387	0.012
#6	0.0523	0.0461	0.001	0.0104	0.0024
#7	0.004	-0.0017	0.0361	0.0023	0.004
#8	0.0154	0.0043	-0.0007	0.0665	0.0006
#9	0.0054	0.0009	0.0038	-0.0246	0.0027
#10	0.0044	0.0002	-0.0765	-0.0025	0.119
#11	0.024	0.0435	0.006	0.0064	-0.0028
#12	0.0751	0.0363	0.0969	0.0835	0.0046

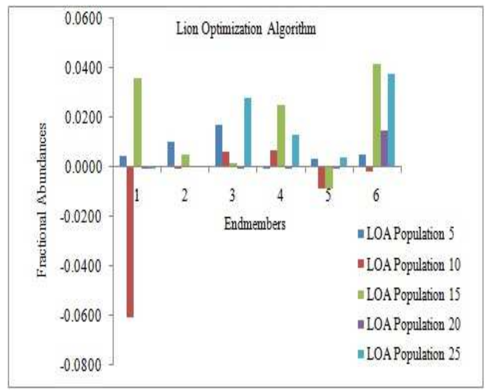

Fgure 8 Performance analysis offractional abundances of endmembers #1 Alunite, #2 Andradite, #3 Buddingtonite, #4 Dumortierite, #5 Kaolinite1, #6 Kaolinite2, #7 Muscovite, #8 Montmorillonite, #9 Nontronite, #10 Pyrope, #11 Sphene and #12 Chalcedony corresponding to Cuprite Image

4.5. Competing methods

Methods such as bi-objective optimization model (Bi-MOSU) and tri-objective optimization model (Tri-MOSU) [11], R-CoNMF [23], Pareto multi-objective based sparse unmixing (Pareto-MOSU) [17], and Rider Optimization Algorithm (ROA) [24] are utilised to compare with the proposed method for the analysis.

4.6. Comparative analysis using the endmembers of images

The comparison of endmembers #1 through #6 of Urban Image is discussed here. Figure 9a, figure 9b, figure 9c, figure 9d, figure 9e and figure 9f, denotes the endmembers of Asphalt, Metal, Roof, Grass, Dirt and Tree endmembers respectively. In figure 9a, the reflectance of the methods Bi-MOSU + Tri-MOSU, R-CoNMF, Pareto-MOSU, ROA, and LA at the band of 48 is -0.0893, -0.0956, -0.5452, -0.4522, and -0.7222,

ISSN: 1992-8645 www.jatit.org E-ISSN: 1817-3195

respectively. It is obvious from the given data that the proposed method has better reflectance when compared to the previous methods. Similarly, when compared to competing approaches, the suggested method outperformed the others for endmembers 2, 3, 4, 5 and 6 respectively. It is obvious that the proposed method outperformed previous research.

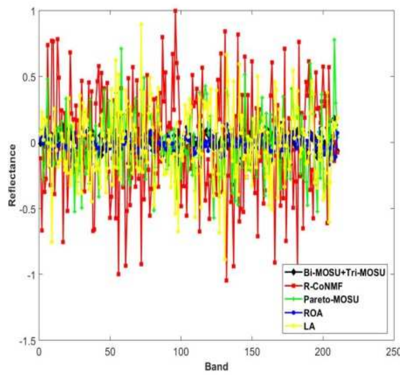

9a. Comparative analysis using Urban endmember #1 (Asphalt)

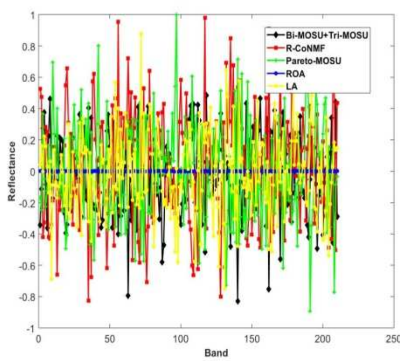

9b. Comparative analysis using Urban endmember #2 (Metal)

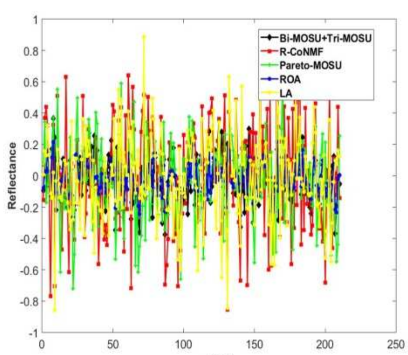

9c. Comparative analysis using Urban endmember #3 (Roof)

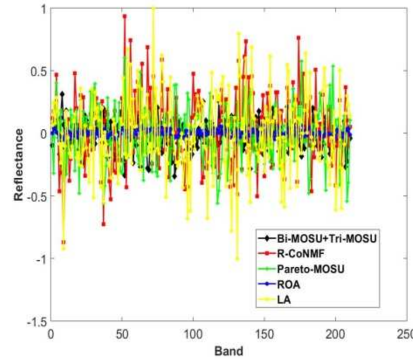

9d. Comparative analysis using Urban endmember #4 (Grass)

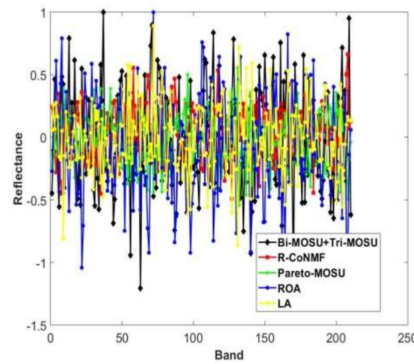

9e. Comparative analysis using Urban endmember #5 (Dirt)

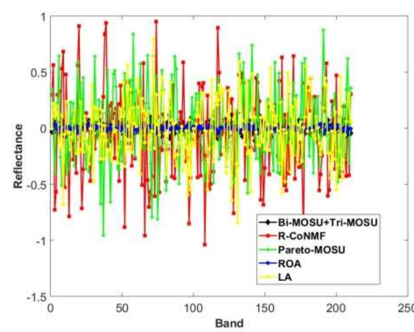

9f. Comparative analysis using Urban endmember #6 (Tree)

The figures 10a through 10l depicts the comparative analysis performed using the endmembers from Cuprite image. The comparative analysis based on the endmembers are depicted in figures 10a, 10b, 10c, 10d, 10e, 10f, 10g, 10h, 10i, 10j, 10k, and 10l respectively. The reflectance of the proposed method, LRO is -0.0417%, 0.0300%, 0.0092%, 0.0453%, -0.0071%, -0.0295%, 0.0211%, 0.0013%, 0.1185%, 0.1427%, -0.0225%, and -0.067%, for the endmembers of original Cuprite image when the band is 224 as per the graphs in figure 10a, figure 10b, figure 10c, figure 10d, figure

ISSN: 1992-8645 www.jatit.org E-ISSN: 1817-3195

10e, figure 10f, figure 10g, figure 10h, figure 10i, figure 10j, figure 10k ,and figure 10l, respectively.

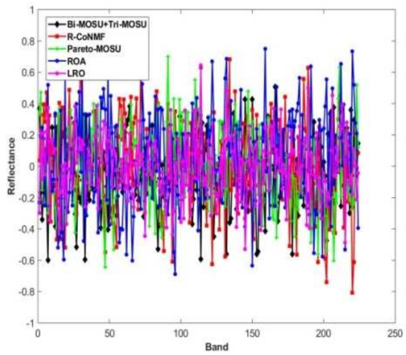

10a. Comparative analysis using Cuprite endmember #1 (Alunite)

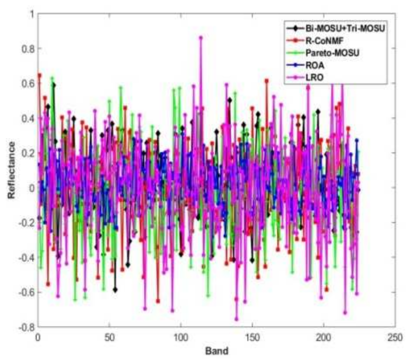

10b. Comparative analysis using Cuprite endmember #2 (Andradite)

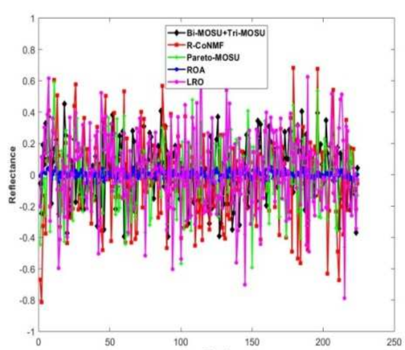

10c. Comparative analysis using Cuprite endmember #3 (Buddingtonite)

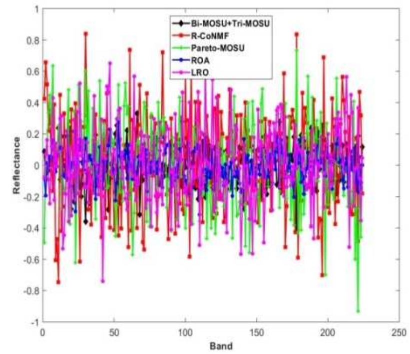

10d. Comparative analysis using Cuprite endmember #4 (Dumortierite)

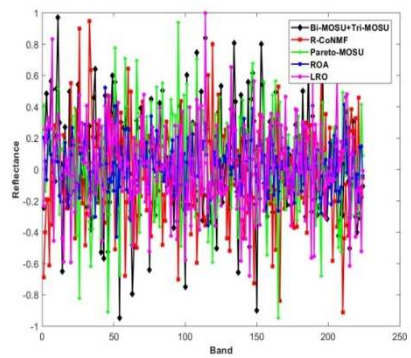

10e. Comparative analysis using Cuprite endmember #5 (Kaolinite1)

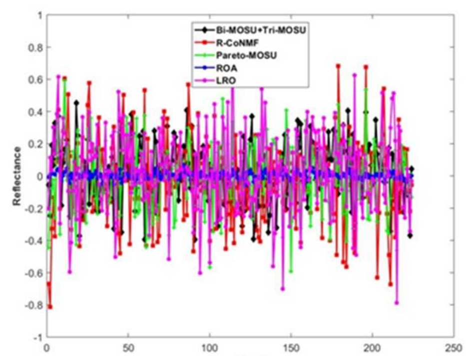

10f. Comparative analysis using Cuprite endmember #6 (Kaolinite2)

ISSN: 1992-8645 www.jatit.org E-ISSN: 1817-3195

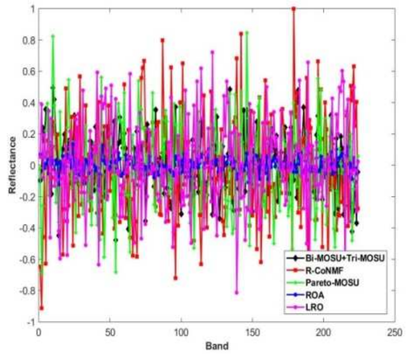

10g. Comparative analysis using Cuprite endmember #7 (Muscovite)

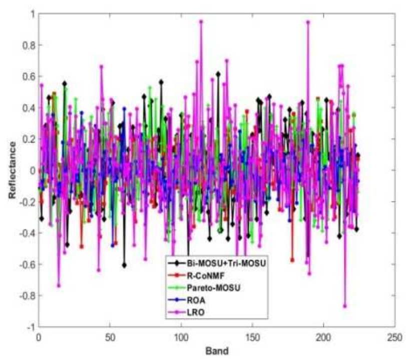

10h. Comparative analysis using Cuprite endmember #8 (Montmorillonite)

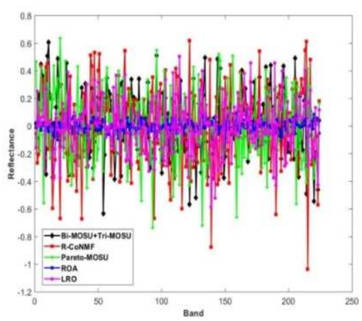

10i. Comparative analysis using Cuprite endmember #9 (Nontronite)

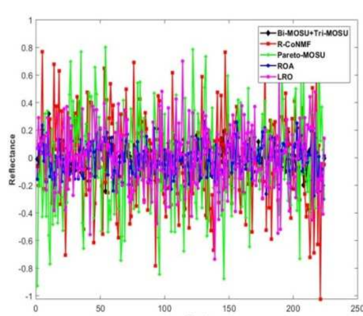

10j. Comparative analysis using Cuprite endmember #10 (Pyrope)

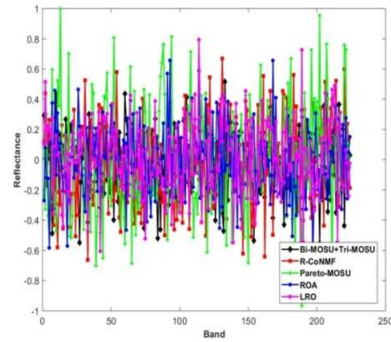

10k. Comparative analysis using Cuprite endmember #11 (Sphene)

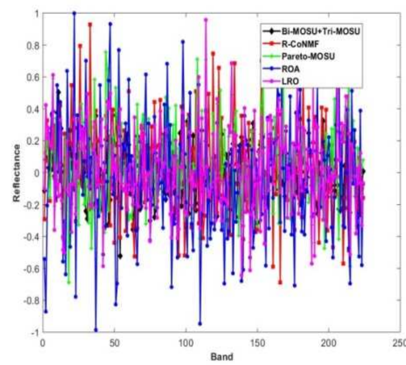

10l. Comparative analysis using Cuprite endmember #12 (Chalcedony)

Figure 10. Comparative analysis of endmembers #1 through #12 of Cuprite image

The comparative analysis based on the performance metrics are demonstrated in this section. Figure 11a through 11d shows the comparative analysis of Urban and Cuprite images based on the performance metrics. Figure 7a shows the comparative analysis using Urban image based on RE. The RE of the methods, Bi-MOSU + Tri-MOSU, R-CoNMF, Pareto-MOSU, ROA, and proposed LRO is 61.2490, 51.4851, 42.7426, 34.7466, and 17.1446 when the SNR is 25dB. Figure 7b shows the comparative analysis using Urban image based on RMSE. The RMSE of the methods, Bi-MOSU + Tri-MOSU, R-CoNMF, Pareto-MOSU, ROA, and proposed LRO is 0.0814, 0.0617, 0.0462, 0.0412, and 0.014 when the SNR is 25dB. Figure 7c shows the comparative analysis using Cuprite based on RE. The RE of the methods, Bi-MOSU + Tri-MOSU, R-CoNMF, Pareto-MOSU, ROA, and proposed LRO is 94.7656, 82.5873,

ISSN: 1992-8645 www.jatit.org E-ISSN: 1817-3195

60.9128, 43.4902, and 19.2401when the SNR is 25dB. Figure 7d shows the comparative analysis using Cuprite based on RMSE. The RMSE of the methods, Bi-MOSU + Tri-MOSU, R-CoNMF, Pareto-MOSU, ROA, and proposed LRO is 0.1255, 0.0807, 0.0576, 0.0533, and 0.0184 when the SNR is 25dB.

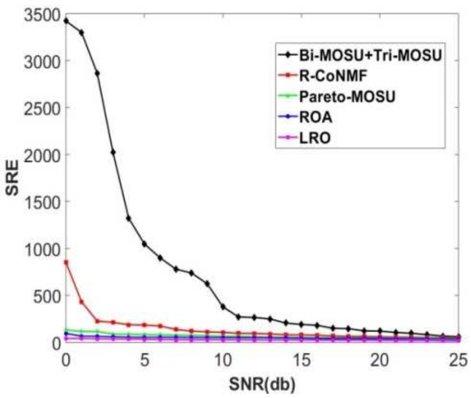

11a. Performance analysis based on Urban SRE

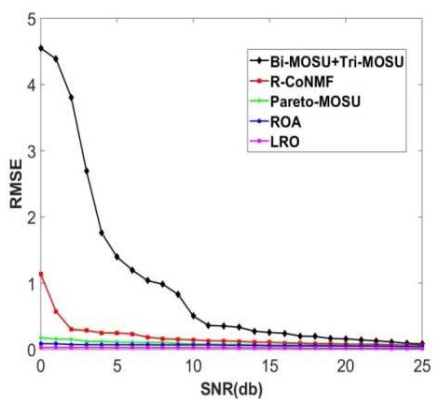

11b. Performance analysis based on Urban RMSE

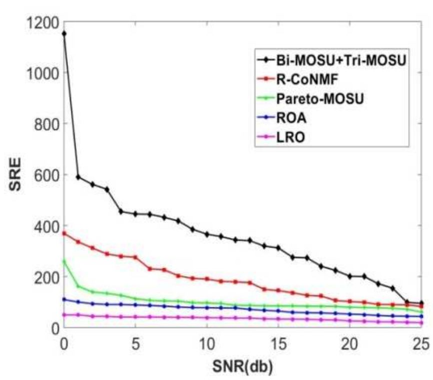

11c. Performance analysis based on Cuprite SRE

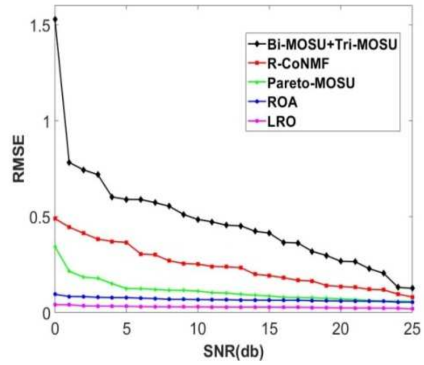

11d. Performance analysis based on Cuprite RMSE

Figure 11. Performance analysis based on SRE and RMSE of both Urban and Cuprite Images

4.7 Analysis using Performance Metrics

Figure 11 illustrates the comparative analysis based on performance metrics in this area. Figure 6 a) shows a comparative analysis based on SRE. When the SNR is 25 dB, the SRE of the methods Bi-MOSU + Tri-MOSU, R-CoNMF, Pareto-MOSU, ROA, and LA is 162.6231, 181.24, 100.12, 103.37, 119.11. Figure 6 b) shows the results of a comparison analysis based on RMSE. When the SNR is 25dB, the RMSE of the methods Bi-MOSU + Tri-MOSU, R-CoNMF, Pareto-MOSU, ROA, and LA is 0.0281, 0.064, 0.0475, 0.0632, and 0.0551. The developed method clearly outperformed the current methods.

4.8. Comparative discussion

Table 3 summarises the debate over the best performance achieved by existing approaches, as measured by SRE and RMSE, respectively. The RE and RMSE metric values for Bi-MOSU + Tri-MOSU are 162.62 and 0.0989, respectively, whereas the RE and RMSE metric values for R-CoNMF are 181.24 and 0.0922. Pareto-RE MOSU's and RMSE values are 100.12 and 0.1429, respectively. Similarly, ROA's RE and RMSE values are 103.37 and 0.0923, respectively. The LA spectral unmixing outperforms the current approaches with a minimum RE and RMSE of 119.11 and 0.0904, respectively, as shown in table 3.

ISSN: 1992-8645 www.jatit.org E-ISSN: 1817-3195

Table 3: Comparative discussion

Methods	RE	RMSE
Bi-MOSU + Tri-MOSU	162.62	0.0989
R- CoNMF	181.24	0.0922
Pareto- MOSU	100.12	0.1429
ROA	103.37	0.0923
Proposed LA	119.11	0.0904

5. CONCLUSION

In order to extract endmembers and fractional abundances from hyperspectral data, this paper provides a Multi-Objective Spectral Unmixing approach for dealing with sparse unmixing. The Multiobjective Lion Optimization approach is used to solve this model. To gain further insight into the sparse unmixing problem, the proposed method optimises the Spatial Neighbor term, Sparsity term, and Reconstruction Error term all at the same time. The multi-objective spectral unmixing technique, which is based on lion social behaviour, aims to attain high accuracy while speeding up convergence. Experimental findings on an urban hyperspectral dataset have demonstrated the technique's utility. In the investigations, the proposed methodology outperformed Bilinear and Trilinear Multi-Objective Spectral Unmixing, Robust Collaborative Nonnegative Matrix Factoriztion, Pareto-Muti-Objective Spectral Unmixing, and Rider Optimization in estimating enhanced endmembers estimation and fractional abundances, with lower Reconstruction Error and Root Mean Square Error values of 119.11 and 0.0904, respectively. Machine learning-based high-performance computing will be investigated in the future for real-time spectral picture interpretation applications, along with the fusion of new nature-inspired computing models, to speed the recommended approach.

REFERENCES:

[1] Abderrahim Halimi, Nicolas Dobigeon, and Jean-Yves Tourneret, "Unsupervised Unmixing of Hyperspectral Images Accounting for Endmember Variability", IEEE Transactions on Image Processing, vol.24,no.12, pp.4904-4917, 2015.

[2] Charis Lanaras, Emmanuel Baltsavias and Konrad Schindler, "Hyperspectral Super-Resolution with Spectral Unmixing Constraints", Remote sensing, vol.9, no.11,pp.1196, 2017.

[3] Rui Wang, Heng-Chao Li, IEEE, Wenzhi Liao, Xin Huang, and Wilfried Philips, "Centralized Collaborative Sparse Unmixing for Hyperspectral Images", IEEE Journal of Selected Topics In Applied Earth Observations And Remote Sensing, vol.10, no.5, May 2017.

[4] Tsung-Han Chan, Chong-Yung Chi, Yu-Min Huang, and Wing-Kin Ma," A Convex Analysis-Based Minimum-Volume Enclosing Simplex Algorithm for Hyperspectral Unmixing", IEEE Transactions on Signal Processing, vol. 57, no. 11, November 2009.

[5] Abderrahim Halimi, Yoann Altmann, Nicolas Dobigeon, andJean-Yves Tourneret," Nonlinear Unmixing of Hyperspectral Images Using a Generalized Bilinear Model", IEEE Transactions on Geoscience And Remote Sensing, vol. 49, no.11, November 2011.

[6] Nicolas Dobigeon, Saïd Moussaoui, Martial Coulon, Jean-Yves Tourneret, and Alfred O. Hero, "Joint Bayesian Endmember Extraction and Linear Unmixing for Hyperspectral Imagery", IEEE Transactions on Signal Processing, vol. 57, no. 11, November 2009.

[7] Zuyuan Yang, Guoxu Zhou, Shengli Xie, Shuxue Ding, Jun-Mei Yang, and Jun Zhang, "Blind Spectral Unmixing Based on Sparse Nonnegative Matrix Factorization", IEEE Transactions on Image Processing, vol. 20, no. 4, April 2011.

[8] Yoann Altmann, Abderrahim Halimi, Nicolas Dobigeon, and Jean-Yves Tourneret, "Supervised Nonlinear Spectral Unmixing Using a Post nonlinear Mixing Model for Hyperspectral Imagery",IEEE Transactions on Image Processing, vol.21, no. 6, June 2012.

[9] Yoann Altmann, Nicolas Dobigeon and Jean-Yves Tourneret, "Bilinear Models for Nonlinear Unmixing of Hyperspectral Images", In Hyperspectral Image and Signal Processing: Evolution in Remote Sensing (WHISPERS), IEEE, pp. 1-4, June 2011.

[10] José M. Bioucas-Dias, Antonio Plaza, Nicolas Dobigeon, Mario Parente, QianDu, Paul Gader, and Jocelyn Chanussot," Hyperspectral Unmixing Overview: Geometrical, Statistical, and Sparse Regression-Based Approaches", IEEE Journal of Selected Topics in Applied Earth Observations And Remote Sensing, vol. 5, no. 2, April 2012.

ISSN: 1992-8645 www.jatit.org E-ISSN: 1817-3195

[11]Luo, W., Gao, L., Plaza, A., Marinoni, A., Yang, B., Zhong, L., Gamba, P. and Zhang, B., "A new algorithm for bilinear spectral unmixing of hyperspectral images using particle swarm optimization," IEEE Journal of Selected Topics in Applied Earth Observations and Remote Sensing, vol.9, no.12, pp.5776-5790, 2016.

[12] Michael E. Winter,"N-FINDR: an algorithm for fast autonomous spectral end-member determination in hyperspectral data", In Imaging Spectrometry, International Society for Optics and Photonics, vol. 3753, pp. 266-276, October 1999.

[13]José M. P. Nascimento, and José M. Bioucas Dias, "Vertex Component Analysis: A Fast Algorithm to Unmix Hyperspectral Data", IEEE Transactions on Geoscience and Remote Sensing, vol. 43, no. 4, April 2005.

[14]Joseph W. Eoardman, Fred A. Kruse, Robert O. Green, "Mapping Target Signatures Via Partial Unmixing Of Aviris Data",1995.

[15] Michael Frank and Mort Canty, "Unsupervised Change Detection for Hyperspectral Images", In Proceedings of AVIRIS workshop, February 2003.

[16]Sicong Liu, Lorenzo Bruzzone, Francesca Bovolo, and Peijun Du, "Unsupervised Multitemporal Spectral Unmixing for Detecting Multiple Changes in Hyperspectral Images", IEEE Transactions on Geoscience and Remote Sensing , vol. 54 , no. 5 , pp. 2733 -2748,May 2016.

[17]Xu, X. and Shi, Z., "Multi-objective based spectral unmixing for hyperspectral images", ISPRS Journal of Photogrammetry and Remote Sensing, vol.124, pp.54-69, 2017.

[18]Simon Henrot, Jocelyn Chanussot, and Christian Jutten, "Dynamical Spectral Unmixing of Multitemporal Hyperspectral Images",IEEE transactions on image processing, vol. 25, no. 7, July 2016.

[19]Gong, M., Li, H., Luo, E., Liu, J. and Liu, J., "A multi objective cooperative co-evolutionary algorithm for hyperspectral sparse unmixing," IEEE Transactions on Evolutionary Computation, vol.21, no.2, pp.234-248, 2017.

[20]A. A. Nielsen, "The regularized iteratively reweighted MAD method for change detection in multi- and hyperspectral data," IEEE Trans. Image Process., vol. 16, no. 2, pp. 463–478, Feb 2007.

[21]B R Rajakumar, "Optimization using Lion Optimization Algorithm: a biological inspiration from lion's social behaviour, Evolutionary Intelligence, vol.11, pp.31-52, 2018.

[22]"Urban and Cuprite data" from Remote Sensing Laboratory, School of Surveying and Geospatial Engineering, accessed on 22 September 2021.

[23]Jun Li,José M. Bioucas-Dias, Antonio Plaza, and Lin Liu, " Robust Collaborative Nonnegative Matrix Factorization for Hyperspectral Unmixing", IEEE Transactions on Geoscience and Remote Sensing, vol.54 , no.10, pp. 6076 - 6090, Oct. 2016.

[24]Binu, D. and Kariyappa, B.S., "RideNN: A New Rider Optimization Algorithm-Based Neural Network for Fault Diagnosis in Analog Circuits," IEEE Transactions on Instrumentation and Measurement, 2018.

[25]Wang, D., Shi, Z. and Cui, X., "Robust Sparse Unmixing for Hyperspectral Imagery," IEEE Transactions on Geoscience and Remote Sensing, vol.56, no.3, pp.1348-1359, 2018.

[26]Li, J., Li, H., Liu, Y., & Gong, M. (2021). Multi-fidelity evolutionary multitasking optimization for hyperspectral endmember extraction. Applied Soft Computing, 111, 107713. https://doi.org/10.1016/j.asoc.2021.107713

[26]Wang, Z., Wei, J., Li, J., Li, P., & Xie, F. (2021). Evolutionary multiobjective optimization with endmember priori strategy for large-scale hyperspectral sparse unmixing. Electronics (Switzerland), 10(17), 1–13. https://doi.org/10.3390/electronics10172079

[27]Xu, X., Pan, B., Chen, Z., Shi, Z., & Li, T. (2021). Simultaneously Multiobjective Sparse Unmixing and Library Pruning for Hyperspectral Imagery. IEEE Transactions on Geoscience and Remote Sensing, 59(4), 3383–3395. https://doi.org/10.1109/TGRS.2020.3016941